*Journal of Applied Fluid Mechanics*, Vol. 19, No. 1, pp. 3236-3253, 2026. Available online at <a href="www.jafmonline.net">www.jafmonline.net</a>, ISSN 1735-3572, EISSN 1735-3645. <a href="https://doi.org/10.47176/jafm.19.1.3619">https://doi.org/10.47176/jafm.19.1.3619</a>



# Investigation on the Effect of Impingement Chamber Structure and Cooling Unit Number on Composite Cooling

J. Liu<sup>1,2</sup>, Z. Zhu<sup>2,3</sup>, J. Chang<sup>1,2†</sup>, S. Ma<sup>2,3</sup>, and J. Sun<sup>2,3</sup>

School of Aerospace Engineering, North University of China, Taiyuan, 030051, China
 Research Institute of Intelligent, North University of China, Taiyuan 030051, China
 College of Mechatronics Engineering, North University of China, Taiyuan 030051, China

†Corresponding Author Email: changil@nuc.edu.cn

#### **ABSTRACT**

In order to deeply explore the influence and mechanism of the impingement chamber structure and the number of cooling units on the film cooling performance. Based on the Realizable k- $\varepsilon$  turbulence model with finite volume composite cooling structure as the research object, the cold flow in the cooling structure with different volumes and shapes of impingement chambers and different numbers of cooling units is investigated in this paper. The numerical method is verified by the existing experimental results, and the grid independence analysis is carried out. The changes of flow field structure and cooling effectiveness under different working conditions are comprehensively analyzed. The results indicate that the volume and shape of the impingement chamber influence the flow structure of the cold flow in the chamber, thereby affecting the flow state of the cold flow in the film hole, ultimately resulting in different momentum distributions of the cold flow at the outlet of the film hole. The strength of the kidney-shaped vortex pair on both sides of the film is directly affected by the momentum distribution of the cold flow at this location, leading to the difference in the film cooling flow on the wall. It is found that the composite cooling structure with a volume of  $0.8V_r$  and a circle impingement chamber has better cooling flow ductility and wall adhesion. The momentum distribution of the film hole outlet section of the increased cooling unit is affected by the film flow with regarding the impingement hole, impingement chamber and film hole as a single cooling unit, and the surface-averaged film cooling effectiveness at  $N_u$ =4 is improved by approximately 78.47% compared to  $N_u=1$ .

# Article History

Received April 20, 2025 Revised July 13, 2025 Accepted August 5, 2025 Available online November 5, 2025

### Keywords:

Composite cooling Impingement chamber Cooling effectiveness Cooling flow Kidney-shaped vortex pair

#### 1. Introduction

The turbine inlet temperature of an Aero-engine plays a key role in the increase of its thrust (Bunker, 2007). According to the calculation in reference Boyce (2011), the engine thrust can be increased by 7~8% for every 50°C increase in turbine inlet temperature for the same class of gas turbine with other parameters unchanged. The inlet temperature of modern Aero-engine has exceeded 2200K (Yeranee & Yu, 2021), the excessive turbine inlet temperature is far beyond the thermal limit of the high temperature component materials. At the same time, the improvement of thermal resistance of the high temperature working component materials significantly lags behind the growth rate of the turbine inlet temperature. To ensure stable and reliable

operation of high temperature components, cooling technology must be used. Currently, the gas turbine is mainly cooled by a composite cooling method combining internal flow cooling and film cooling (Unnikrishnan & Yang, 2022).

At present, the internal cooling methods used more often include impingement cooling, turbulent cooling and swirl cooling (Nourin & Amano, 2021). Among them, impingement cooling is the most effective method to increase the local heat transfer coefficient. The cold air passes through the small impingement holes at a very high speed to the inner wall of the blade for effective cooling, then part of the airflow is discharged from the blade through the film holes, and the other part is finally exhausted from the trailing edge of the blade through the internal flow channel.

NOMENCLATURE			
Bi	Biot number	$\mathbf{W}_{\mathrm{j}}$	width of impingement chamber
BR	film cooling blowing ratio	$X^{'}$	X-coordinate
D	diameter of film hole	Z	Z-coordinate
$H_j$	height of impingement chamber	β	impingement inclined angle
$L_{j}$	length of impingement chamber	$\Delta d$	distance between film hole and impact holes
$N_u$	number of cooling units	$\Delta l$	length between the impact holes
$v_c$	velocity of coolant	$\eta$	film cooling effectiveness
$V_r$	volume of the impingement chamber	$\overline{\eta}$	spanwise average overall cooling effectiveness
$V_y$	velocity in y direction	$\overline{\eta}_{ ext{s}}$	surface-averaged film cooling effectiveness
$ u_{\infty}$	velocity of mainstream		

Film cooling is to spray the cold air from the holes or tangent gaps on the surface in the high temperature environment to the mainstream. The cold air will bend and adhere to the wall surfaces under the pressure and friction of the high temperature mainstream. The wall is separated from the high temperature mainstream by a cold air film formed to reduce heat transfer, thermal radiation and corrosion to the wall, while taking away part of the high temperature gas to play a protective role to the wall.

The "impingement-film" composite cooling method can significantly improve the cooling effectiveness of the turbine blades by combining the advantages of the two cooling methods. It is an important means to enhance the cooling effect of the turbine blades, and is widely used in areas with large heat load such as the leading edge of blades (Nathan et al., 2014, Zhang et al., 2022, Cheng et al., 2023).

The research of impingement-film composite cooling technology has been carried out since the 1990s, and a large number of studies have been conducted using experimental and numerical methods. The influence of different impingement plate structures on the cooling performance of turbine blade leading edge was reported by Ravelli et al. (2010). The results showed that the impingement cooling had little effect on the overall cooling effectiveness due to the conjugate effect. Cho and Rhee (2001) studied the heat transfer effect of impingement-film composite cooling structure by changing the geometrical and aerodynamic parameters. It was found that the heat transfer effect near the shock stagnation zone was the best if there was an optimal impingement spacing, and increasing Re was beneficial to enhance the heat transfer effect. The arrangement between the impingement holes and the film holes would greatly affect the heat transfer effect. Ligrani et al. (2017) investigated the influence of the height of the spoiler column on the heat transfer capacity of the impingement cooling structure, and found that the change of the height of the circular spoiler column could enhance the heat transfer capacity of the target surface to varying degrees.

The cooling performance of the composite cooling structure with a small number of impingement holes versus a large number of air-film holes was investigated by EI-Jummah et al. (2017). It was revealed that increasing the number of film holes or decreasing the hole spacing was favorable to the effectiveness of the cooling structure. Yang et al. (2013) used eight film

cooling methods to establish a 2/3 cylindrical leadingedge model with three exhaust film holes. It was noticed that the film suction could not only strengthen the local heat transfer, but also restrict the wall jet. The position of the film hole had a significant effect on the shape of the high heat transfer zone and the cooling of the intermediate zone. Liu et al. (2020) and, Liu, Y. et al. (2021) studied the heat transfer performance and flow field distribution of double wall cooling system under different blowing ratios, aspect ratios and film hole arrangements. The results showed that the cooling effectiveness of hexagonal film holes was 24.5% higher than that of linear film holes when Bi=0.56.

Xiao-ming et al. (2015) and Luan et al. (2023) found that the cooling effect of the impingement-film structure was better arranged in a cross row rather than a straight row, and reducing the distance between the impingement holes could also improve the overall heat transfer effectiveness. Biased jet had better cooling effect, and the ridge ribs on the impact target surface could improve the uniformity of coolant distribution. The effect of adding pits to the target surface of a composite cooling structure on heat transfer and cold flow was analyzed by Luo et al. (2016) and Kalghatgi and Acharya (2015). It was observed that the heat transfer performance of the composite cooling structure was improved by 15.8% by increasing the diameter and depth of the pits compared with that without pits at high Re. However, further increasing the size of the pits would lead to a decline in heat transfer performance. Yang et al. (2016) combined the composite cooling structure of the cylindrical cold air chamber with the ramp structure, and investigated the influence of the ramp angle and the inclination angle of the impingement hole of the structure on the cooling effectiveness. The inclination angle of the impingement hole will affect the strength of the swirling flow in the chamber, and the ramp can effectively expand the film coverage. Singh (2022) investigated the flow and heat transfer of film cooling with positive and negative holes, and found that impingement-film composite cooling could improve the heat transfer performance and cause higher pressure loss. Liu, X. et al. (2021), and Li et al. (2022) observed the influence of pore size and thermal conductivity on the heat transfer performance of double wall with needles, and the difference in cooling characteristics between impingement/film composite cooling and cyclonic impingement/film composite cooling. The results showed that higher thermal conductivity and larger film hole size were beneficial to improve the film cooling effect. The overall average cooling effectiveness of cyclonic impingement/film composite cooling was increased by more than 6% compared to impingement/film composite cooling.

It can be observed that the impingement-film composite cooling structures based on double wall cooling systems have been extensively investigated from the references above. These investigations primarily focus on modifying the arrangement patterns and spacing of impingement holes and film holes. Additional efforts involved are working on increasing spoiler components and other ways to enhance target surface heat transfer capacity and improve overall cooling performance. Existing research on composite cooling structures mainly focuses on exploring the relevant parameters or arrangement methods of air film holes (Li et al., 2017, Bunker, 2005, Liu et al., 2020, Schmidt, et al., 1996). However, the core role of the volume and shape of the impingement chamber in regulating the momentum distribution of cold flow has not been studied, and there are few studies on the array effect of cooling units.

To fill this gap and explore composite cooling structures with higher efficiency, this paper investigates the finite-volume composite cooling structure as the research object and establishes the correlation mechanism between "cavity structure-cold flow rate-air film cooling performance". The study is the first to explore the coupling mechanism of impact cavity volume and shape on cold flow and film cooling efficiency, study the influence of cooling unit number on air film momentum distribution, and introduce the correlation between kidney-shaped vortex intensity and wall air film coverage. This provides clear structural parameter guidance for optimizing cooling solutions for high heat load components such as turbine blades in aircraft engines.

# 2. NUMERICAL METHODS

In this paper, the solver FLUENT 2020 R1 is used to solve the problem, and the correlation between the flow field structure and the film cooling performance in the composite cooling structure is studied. The reproducible parameters related to algorithms, methods, and criteria are as follows. A pressure-based solver is used to achieve the pressure-velocity coupling, and the SIMPLE algorithm is used for the pressure velocity coupling. For spatial discretization, the gradient is calculated based on the Least Squares Cell-Based method. The Second-Order Upwind scheme is used for other discrete schemes such as pressure, momentum and turbulent kinetic energy. The relaxation factors of momentum, turbulent kinetic energy and energy are 0.7, 0.8 and 1, respectively. When the normalized residuals of all governing equations are less than 10<sup>-7</sup>, the simulation is judged to be convergent. The above data and details ensure that the results are reproducible.

The Realizable k- $\varepsilon$  turbulence model can accurately predict the dispersion ratio of the jet in the plate and cylinder region, and possesses higher precision when dealing with complex flows. Further, the conditions of

rotational flow and boundary layer flow under strong inverse pressure gradient are also better simulated by the model. Therefore, the Realizable k- $\varepsilon$  model is selected for numerical simulation in this paper. The turbulent model equations and definitions of some parameters and terms used in this paper are given in the appendix.

#### 2.1 Grid Independence Verification

ICEM is used to generate the structured grid of the computational domain shown in Fig. 1. The computational domain consists of about 3.28 million hexahedral structured grids, with the dimensions of 60D  $\times 5D \times 10D$  along the flow direction, spanwise direction and normal direction respectively. The establishment of this region refers to the setting standard of Zhang et al., 2023, which is large enough to ensure the sufficient development of cold flow while avoiding the influence of the boundary of the calculation region on cold flow. Taking into account the separation of fluid and boundary layer as well as the amount of calculation, the grid element size around the orifice is linearly increased to aperture D in the proportion of 1.08. The  $y^+$  value near the wall is close to 1, which is based on the requirement of analyzing the viscous bottom layer. In addition, the grid near the plate wall is refined. The node growth rate between two adjacent grids at any position is maintained within 0.7~1.3 in order to improve the computational accuracy, as shown in Fig. 1.

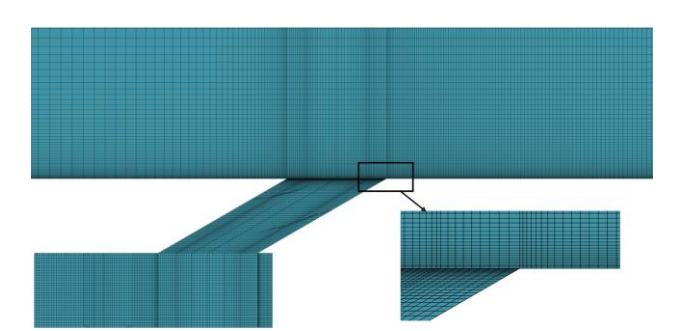


Fig. 1 Schematic diagram of grid division in computational domain

The specific boundary conditions and parameter settings for grid independence verification are the same as in Section 3.1.1, and the impingement chamber volume is taken as  $V_r$ . In order to ensure the accuracy of numerical simulation, three different grid numbers of 2.3 million, 3.28 million and 4.43 million were used to verify the grid independence in the calculation domain established above. The 2.3 million grid is based on the preliminary estimation of the wall boundary layer thickness in the calculation domain, which can basically meet the calculation requirements in the mainstream region. The 3.28 million grid is locally densified near the wall and the impingement chamber based on the 2.3 million grids. The 4.43 million grid is used as the control group of the refined grid, and the number of grids in the above areas is mainly increased.

The grid independence comparison results are shown in Fig. 2. The three curves in the figure represent the relationship between wall temperature and position for

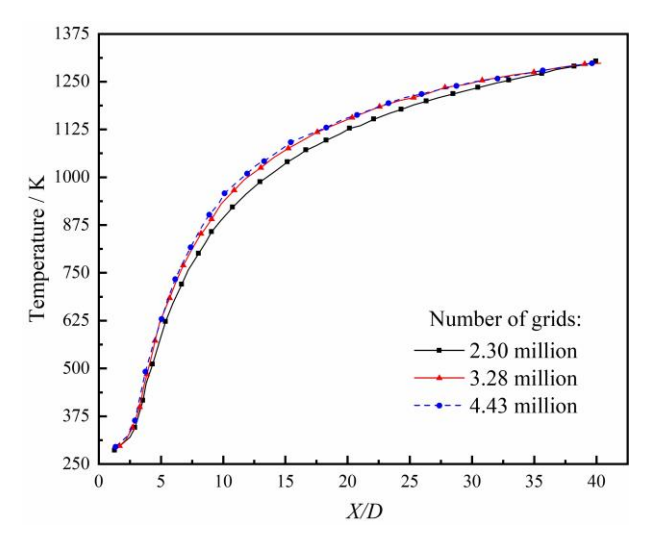


Fig. 2 Grid independence comparison results

different grid numbers. The ratio of the distance in the flow direction starting from the orifice to the diameter of the film orifice is taken as the horizontal axis. It can be noticed from the figure that in the region of 1 < X/D < 40 flow field, there is a significant deviation between the results of 2.3 million and 3.28 million grids, while the little difference between the calculation results of 3.28 million and 4.43 million grids is observed. In other words, 3.28 million grids are sufficient to resolve the flow field without causing inaccuracy in the calculation results, which proves that the calculation results are independent of the flow field grid. For other operating conditions, the number of grids should be close to 3.28 million.

# 2.2 Model Accuracy Validation

In this section, the Realizable k- $\varepsilon$  turbulence model is selected for simulation calculations, and the results of Zhang (Zhang et al., 2023) are used to compare and verify the simulation results.

Figure 3 shows the data comparison between this paper and Zhang at mainstream inlet velocity of 12 m/s, temperature of 323K, coolant temperature of 303K, BR=1,  $Bi=\infty$  and  $\beta=30^{\circ}$ . The gray area indicates the position of film holes on the wall. Obviously, the simulation results are in good agreement with Zhang's data, which verifies the accuracy of the computational model and numerical method, and ensures the credibility of the model calculation results in the subsequent research.

# 3. RESULTS AND DISCUSSION

# 3.1 Investigation of the Effect of Impingement Chamber Volume on Composite Cooling Flow

## 3.1.1 Physical Model and Boundary Condition

In the three-dimensional flow field of film cooling, the cross sections of both film hole and impingement holes are set to be circular with diameters of D and 0.3D, incidence angles of  $30^{\circ}$  and  $90^{\circ}$ , and lengths of 3D and 1.5D, respectively. The mainstream chamber is rectangular with length, width and height of 60D, 5D and

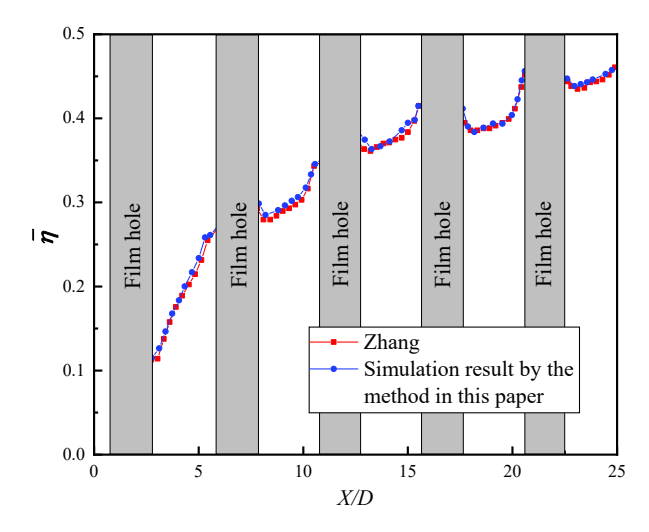
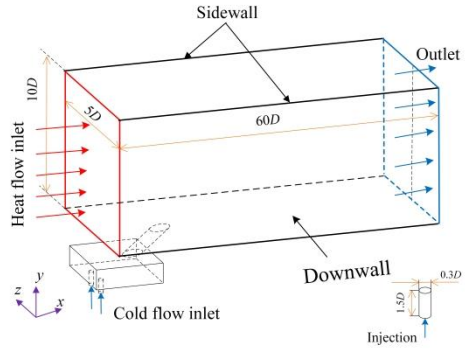
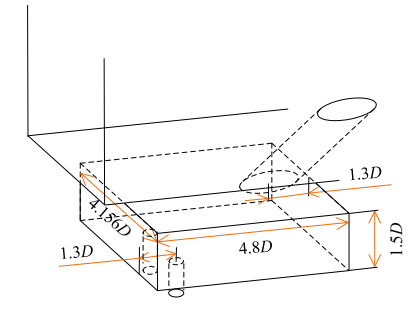


Fig. 3 Model accuracy validation results



(a) Schematic diagram of the calculation domain



(b) Impingement chamber size

Fig. 4 Schematic diagram of physical model

10D respectively. The dimensions of impingement chamber are  $L_i=4.156D$ ,  $W_i=4.8D$ , and  $H_i=1.5D$ . The distance between the impingement hole and the film hole orifice and the walls on both sides of the impingement chamber is 1.3D. The lateral heat flow is 10D away from the air film orifice. The three-dimensional schematic diagram of the calculation domain is shown in Fig. 4(a), and the boundary conditions of the simulation are shown in Table 1. The size of the calculation area is large enough to ensure the full development of the cool flow. This will cover the range of the cold flow from the film hole into the mainstream chamber to the full development, while avoiding the influence of the boundary of the calculation area on the cold flow. The flow direction distance between the film hole and the impact hole  $\Delta d=2.2D$ . The distance between the impact

Table 1 Boundary conditions of the simulation

Name	Boundary condition
Inlet	Velocity inlet
Sidewalls	Periodic wall
Outlet	Pressure outlet
Down wall	Cooling stave surface
The other walls	Adiabatic, non-slip wall

holes  $\Delta l=1D$ , and they are symmetrically distributed along the transverse axis of the film holes.

Both hot flow and cold flow are incompressible ideal gases with density of 1.225kg/m³, temperatures of 1500K and 298.15K, velocities of 12 m/s and 6 m/s, respectively. The blowing ratio remains BR=2 uniformly.

In this paper, the volume  $V_r$  of the impingement chamber is varied by changing the length of the long side of the chamber, and the lengths of other sides remains unchanged, that is,  $nV_r = nL_i \times W_i \times H_i$ .

# 3.1.2 Effect of Impingement Chamber Volume on Cooling Flow

As can be seen from Fig. 5, when the cold flow enters the impingement chamber vertically and impinges the upper wall surface, the flow state of the cold flow changes and is dispersed into multiple tributaries. According to the motion state, they can be divided into two categories, one is that the tributary directly flows into the film hole along the upper wall of the impingement chamber with the velocity along the positive *x* direction. The majority of the cold flows exhibit the other movement state, with non-*x* positive direction velocity. In the initial stage, they move towards their respective velocity direction and hit the side wall or bottom surface. The cold flows between the impingement holes interfere with each other, and change the

movement direction again when reaching the inner surface. The velocity of the cold flow decreases when its state of motion is in the process of varying and finally flows into the film hole under the action of pressure. Since the impingement chamber is symmetrical about the *xoy* plane, an approximately symmetrical flow structure is eventually generated in the chamber.

There are differences in the final state of cold flow in chambers with different volumes. For the chamber with a volume of  $0.5V_r$ , part of the cold flow forms a strong vortex around the z axis in the negative x direction due to the long narrow shape of the chamber. This part of stream strikes at the upper surface again, then flows to the side wall in the positive x direction like other cold flows. Ultimately it enters the film hole under the pressure. For the chambers with volumes of  $0.8V_r$  and  $1.0V_r$ , the volume of the chamber is slightly expanded, so that a vortex with less intensity is generated by the cold flow in the negative x direction. The cold stream is affected by the part of the flow moving in the positive xdirection and bound by the inner surface on both sides in the z direction when it impinges on the upper surface again and the vortex rotation axis turns to the x axis. For the chambers with volumes of  $1.5V_r$ ,  $2.0V_r$  and  $3.0V_r$ , the volume of the chamber is further expanded, so that a vortex with low intensity is also formed by the cold flow in the negative x direction. Due to the growth of the long side, the vortex moving in the positive x direction is no longer bound by the walls on both sides in the z direction, and the cold flow escapes on both sides. Finally, it converges into the film hole under the pressure.

Figure 6 presents the streamline distribution and velocity contour at the center section of the composite cooling structures with different volumes. As shown, the rectangular dashed box is the high momentum area inside the impingement chamber, and the red elliptical dashed box contains the low momentum region of the film hole.

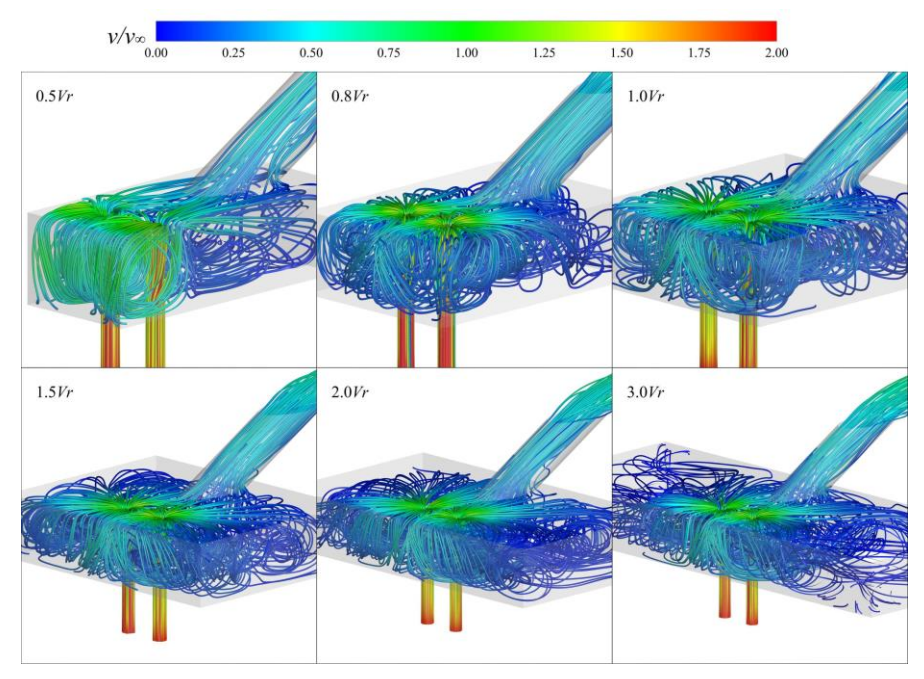


Fig. 5 Three-dimensional velocity streamline distribution in impingement chambers with different volume

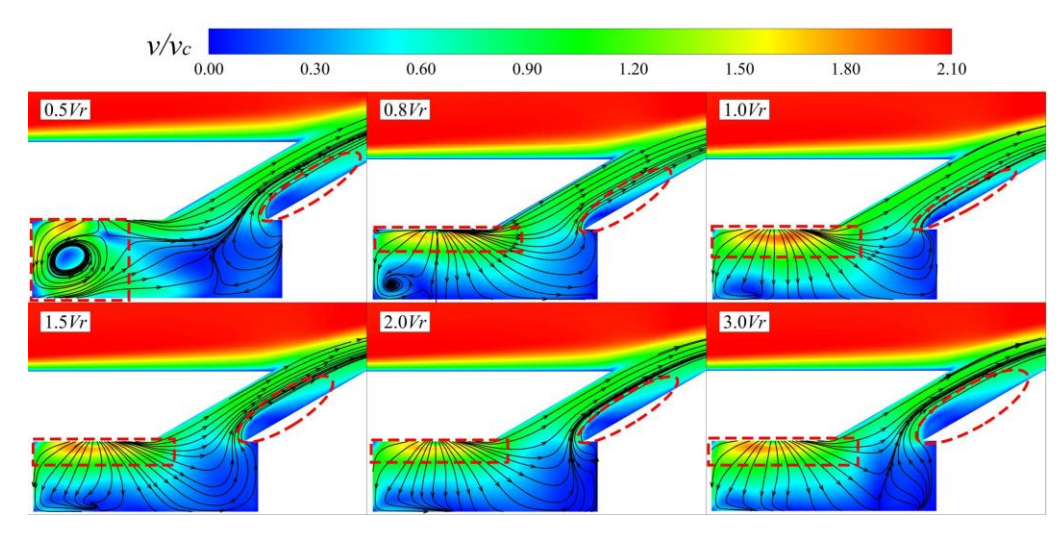


Fig. 6 Streamline distribution and velocity contour at the center section of composite cooling structures with different volumes

From the streamline distribution at the central section of the composite cooling structure, it can be found that the in the chamber with a volume of  $0.5V_r$ , a strong vortex is generated by the cold flow near the side wall in the negative x direction. The cold flow rotates around the vortex and moves toward the film hole, squeezes with the reflux flow impinging on the side wall surface in the positive x direction, and finally converges into the film hole. At the same position of the chamber with volume  $0.8V_r$ , a vortex structure with lower intensity and a closer core to the lower wall surface is generated. The rest of the cold flow is as depicted in Fig. 6. The cold flow moves along the speed direction after impacting the upper wall, and flows into the film hole along the side wall under the effect of pressure after impacting the lower wall and the side wall. The streamline distribution of the chambers with the volume of  $1.0V_r$ ,  $1.5V_r$ ,  $2.0V_r$  and  $3.0V_r$  is similar, and no vortex structure is generated at the center section after the cold flow impinges on the upper wall. With the increase of the chamber volume, the backflow is generated on the side wall in the positive x direction of the chamber with the volume of  $2.0V_r$  and  $3.0V_r$ , and the return flow region expands with the increase of the volume.

Comparing the velocity distribution cloud diagram in the center section of the composite cooling structure, the chamber with a volume of  $0.5V_r$  has a large range of high momentum region mainly at the periphery of the vortex. In other case, a class of rectangular high momentum region exists on the upper wall of the chamber, and the cold flow located in the red rectangular region has greater kinetic energy.

There are differences in the cold flow structure within each impingement chamber. Due to the differences in the acceleration and separation of the cold flow, an obvious low momentum zone is generated at the entrance of the film hole. Comparing the film hole area in Fig. 6, two cold flows in the chambers with volumes of  $0.5V_r$ ,  $1.5V_r$ ,  $2.0V_r$ , and  $3.0V_r$  squeeze and converge with each other to form a high momentum air flow into the film hole, and the streamline distribution around the low momentum area is relatively dense. In contrast, there

is no cold flow convergence at the entrance of the film hole in the chambers with volumes of  $0.8V_r$  and  $1.0V_r$ , and the streamline distribution in the low momentum region in the film hole is relatively sparse. From the elliptical region on the lower wall of the film hole, when the volume of the impingement chamber increases from  $0.5V_r$  to  $0.8V_r$ , the low momentum region compresses toward the lower wall of the film hole and the region area decreases. When the volume of the impingement chamber increases from  $0.8V_r$  to  $3.0V_r$ , the low momentum region begins to expand and the region area increases.

Figure 7 illustrates the velocity distribution in the *y* direction at the outlet section of the film hole in composite cooling structures with different volumes. The ability of the cold flow to penetrate the heat flow boundary layer is determined by its *y* direction velocity. In this paper, the green and yellow regions around the film hole are considered to be low momentum regions with velocities less than 2 m/s. The orange region stands for the medium momentum region with velocities from 2 to 2.25 m/s. The orange-red region represents a higher momentum region with velocities of from 2.25 to 2.5 m/s. The red block denotes a high momentum region with velocities more than 2.5 m/s.

The velocity distributions in the y direction at the outlet section of the film holes are approximately symmetrical about the x axis from Fig. 7. However, the cold flow structure in the chamber is not strictly symmetrical, leading to local differences in the y direction velocity distribution. The area of the low momentum region changes with the chamber volume as follows: the area is smallest at  $0.8V_r$ , followed by  $0.5V_r$ . When the volume increases from  $0.8V_r$  to  $3.0V_r$ , the area increases, and the yellow area at  $3.0V_r$  is approximately twice as large as at  $0.8V_r$ . This trend is consistent with the change in the low momentum region in Fig. 7. The area of the medium momentum region varies with chamber volume as follows: the area is close at  $0.5V_r$  and  $0.8V_r$ , slightly larger at  $1.0V_r$  and  $2.0V_r$ , and relatively larger at  $1.5V_r$  and  $3.0V_r$ . In the area of higher momentum region, the volume is the largest at  $0.8 V_r$ ,

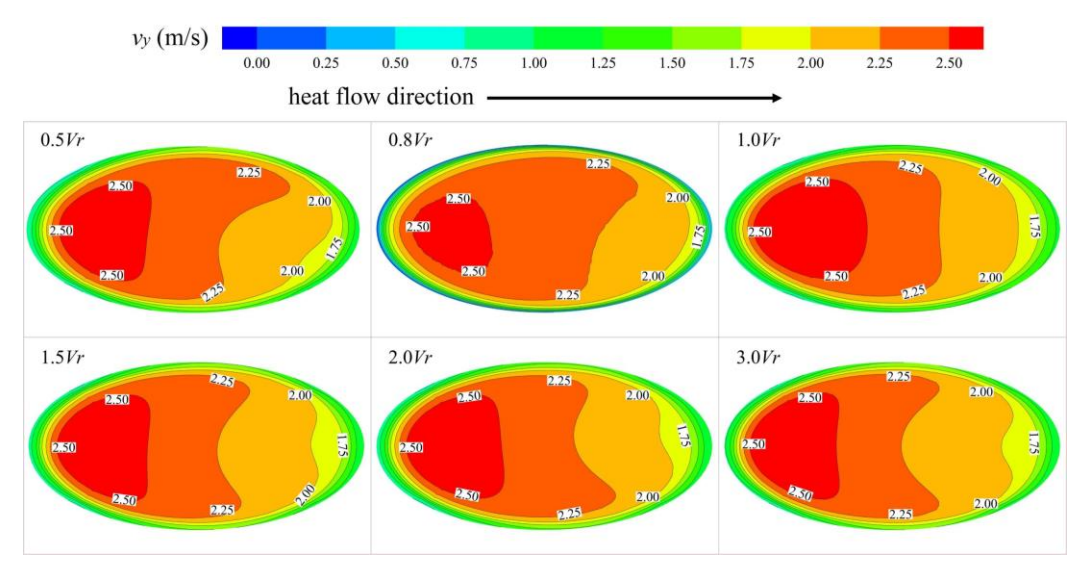


Fig. 7 Velocity distribution in the *y* direction at the outlet section of film hole in composite cooling structures with different volumes

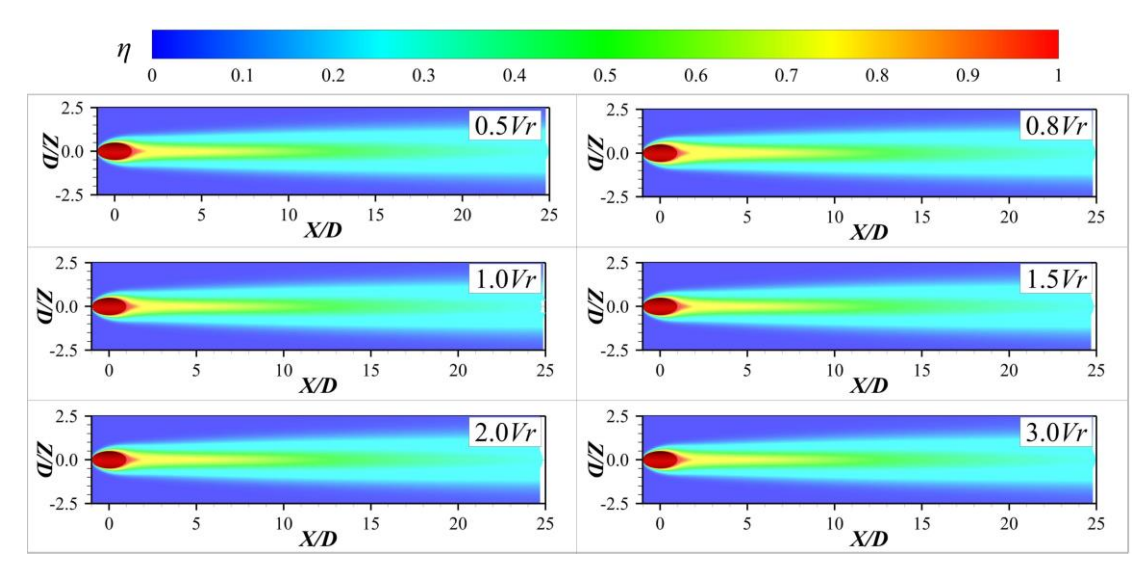


Fig. 8 Cooling effectiveness cloud of flat plate wall of composite cooling structures with different volumes

slightly smaller at  $0.5V_r$  and  $2.0V_r$ , and the smallest at  $1.0V_r$ ,  $1.5V_r$ , and  $3.0V_r$ . The area of the high momentum region shows the opposite trend, the volume is the smallest at  $0.8V_r$ , the largest at  $1.0V_r$ , and the  $0.5V_r$ ,  $1.5V_r$ ,  $2.0V_r$ , and  $3.0V_r$  are essentially the same. Both Fig. 7 and Fig. 8 show that when the volume increases from  $0.8V_r$  to  $1.0V_r$ , the area of high momentum region increases. But when the volume is  $1.5V_r$ ,  $2.0V_r$ , and  $3.0V_r$ , its area decreases compared to  $1.0V_r$ .

Compared with the cloud of cooling effectiveness in Fig. 8, the cooling effectiveness of the air film changes significantly in the area of X/D < 10 on the plate wall. Based on the distribution of red and yellow areas at the outlet of the air film holes, the area of the red region is basically the same in each volume. At  $0.8V_r$ , the yellow area covers a wider region in the spreading direction. At  $0.5V_r$ , the yellow area decreases slightly. The change trend of film cooling effectiveness in other areas is consistent and the area covered is basically the same.

Figure 9 demonstrates the distribution of average cooling effectiveness along the flow direction of composite cooling structures with different volumes. The change of the chamber volume has little effect on the distribution trend of the cooling effectiveness of the composite cooling structure on the plate wall. Across the plate wall, the average cooling effectiveness of the composite cooling structure with a volume of  $0.8V_r$  is the highest, and it is similar for other cases. According to the average cooling effectiveness curve in the 1<X/D<25 region, the average cooling effectiveness curve with a volume of  $1.0V_r$  is at the bottom, the cooling effectiveness curve with a volume of  $0.5V_r$  is just below the  $0.8V_r$  curve, and the  $1.5V_r$  and  $3.0V_r$  curves almost coincide. Further comparing the surface-averaged cooling effectiveness, in the 1<X/D<50 region, the volume improved by about 0.79% at  $0.5V_r$  and 2.85% at  $0.8V_r$  compared to  $1.0V_r$ . In the area of 1 < X/D < 25, the volume increased by about 1.09% at  $0.5V_r$  and 3.96% at  $0.8V_r$ , compared to  $1.0V_r$ .

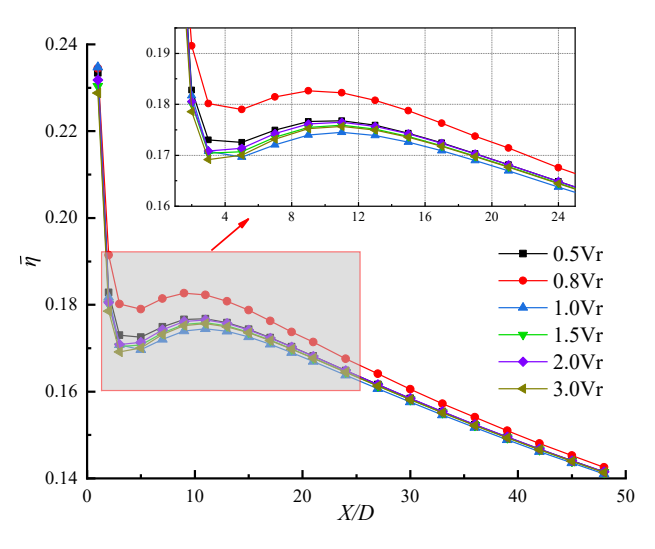


Fig. 9 Distribution of average cooling effectiveness along the flow direction of composite cooling structures with different volumes

According to the analysis of Fig. 7 and Fig. 8, the area of the high momentum region is the smallest at a chamber volume of  $0.8V_r$ , the largest at  $1.0V_r$ , and the remaining four are closer. In the cooling effectiveness cloud chart, the yellow area at  $0.8V_r$  has the largest coverage in the spreading direction, while the yellow region at  $0.5V_r$  slight decreases. The yellow areas under the other four chamber volumes show little difference, indicating that the cooling effect of the film on the flat wall is greatly affected by the size of the high momentum area at the outlet of the film hole. The larger the range of high momentum area, the worse the film cooling effect. And the velocity distributions in the y direction of the film hole outlet section with the volume of  $1.5V_r$  and  $3.0V_r$  are nearly identical, resulting in average cooling effectiveness curves that overlap almost completely.

# 3.2 Investigation of the Effect of Impingement Chamber Shape on Composite Cooling Flow

# 3.2.1 Physical Model and Boundary Condition

Based on the results of numerical simulation and analysis in Section 3.1, the volume of the impingement chamber is maintained at  $0.8V_r$  to optimize the cooling effectiveness. Where the holding height  $H_j$ =1.5D, the blowing ratio BR=2, and other conditions are the same as Section 3.1.

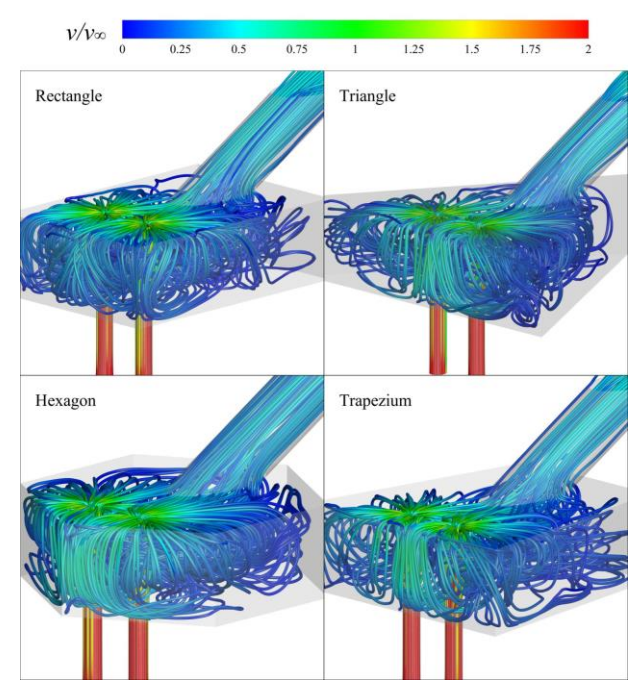
In this study, the selection of polygonal (rectangle, triangle, hexagon and trapezium) and curved (semicircle, flat-key, circle and ellipse) impingement chamber shapes were primarily based on mechanical performance and fluid dynamics considerations. Specifically, triangles have higher strength and stiffness. The hexagonal impingement chamber can form a strong and middle vortex, which makes the cold flow evenly enter the membrane hole. Rectangles are well stabilized and combinable, and the bottom can provide good support. In addition, the plate processing of polygonal impingement chamber is simple, which is suitable for large-scale production of traditional manufacturing process. According to the Coanda effect, the fluid will tend to

flow with the surface of the protruding object, so the smooth curved surface of the curved impingement chamber can guide the fluid to flow smoothly, reduce the flow separation phenomenon (Seok, 2024). And the smooth curved wall can reduce the stress concentration. The circle has the characteristics of uniform distribution of force due to its axial symmetry. In terms of results, it is better suited to resist external and internal pressures. The curved impingement chamber can be manufactured die forming, spinning forming, additive manufacturing and other technologies. In the actual industrial scene, flexibility in selecting appropriate shape of impingement chamber to meet the requirements based on specific space constraints and performance requirements is necessary.

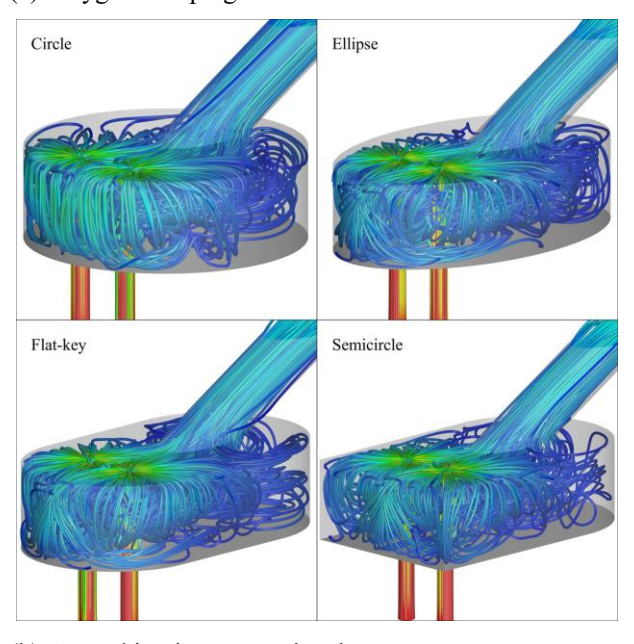
# 3.2.2 Effect of Impingement Chamber Shape on Cooling Flow

Figure 10 exhibits the three-dimensional velocity distribution different polygonal streamline of impingement chambers. In the four different polygonal chambers, the vortex is generated at the position close to the wall in the negative x direction after the cold flow impacts the upper wall, which is limited by the side wall. Based on the color distribution of the velocity streamlines in the vicinity of the vortex, the vortex intensity of hexagon chamber is the largest, the vortex intensity of trapezium and triangle chambers is relatively weak, and the vortex intensity of rectangle chamber is the smallest. In addition, the cold flow always develops around the horizontal vortex in the negative x direction along the sidewalls of the chamber towards the inlet of the film hole for differently shaped chambers. For rectangle chamber, a spiral upward vortex is generated on the wall in the positive x direction of the film hole. In the area near the corners of the triangle chamber, the cold flow is limited by the angle between the adjacent side walls of the chamber, creating a small vortex, but not a spiraling vortex. The axis of the vortex in the hexagon chamber is an arc, the cold flow moves along the side wall, and a spiral upward vortex is generated on the wall in the positive x direction of the film hole. On both sides of the trapezium chamber, two vortices are formed that are closely attached to the sides. At the same time, due to the binding effect of the trapezoid, the cold flow develops towards the upper surface near the film hole, and a spiral upward vortex is formed.

As shown in Fig. 10, similar to the polygonal impingement chamber, in the four curved impingement chambers, after the cold flow impacts the upper wall, the vortex is formed in the negative x direction close to the wall by the restriction of the side wall. The circle chamber exhibits the highest vortex strength, followed by the ellipse and flat-key chambers with moderately while semicircle vortex, the demonstrates the lowest vortex intensity. In four different curved chambers, the cold flow develops along the side wall of the chamber towards the inlet of the film hole around a horizontal vortex in the negative x direction. The presence of the curved sidewalls near the film hole causes more pronounced spiral rising vortices to be formed within the chamber.



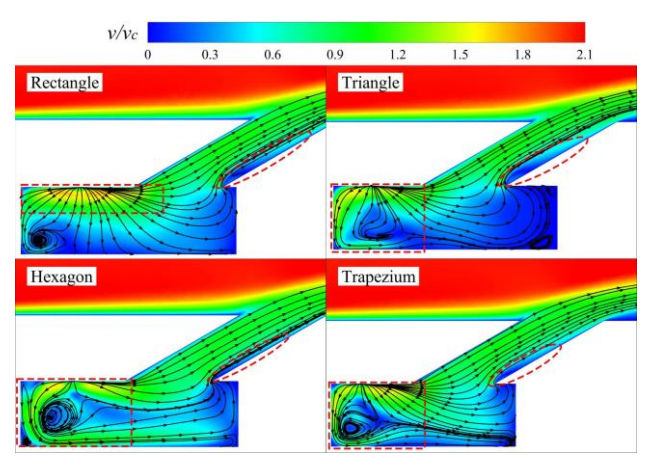
(a) Polygonal impingement chamber



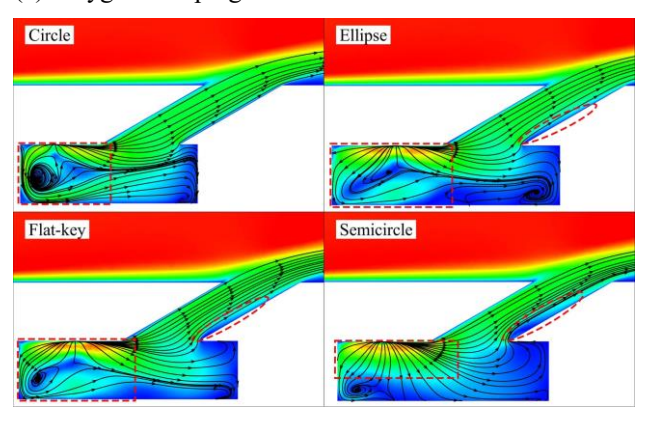
(b) Curved impingement chamber

Fig. 10 Three-Dimensional Velocity Streamline Distribution of Different Impingement Chambers

As seen in Fig. 11(a), vortices are generated in the cold flow near the side wall in the negative *x* direction in the rectangular, hexagon and trapezium chambers. The vortex with low strength in the rectangular chamber is close to the lower wall of the chamber. The vortex nucleus of the hexagon cavity is located at its center with a larger intensity. In the trapezium chamber, the position of vortex core is inclined to the lower wall. In the triangle chamber, only a tiny vortex is formed at the lower right of the impingement position of the upper wall. Unexpectedly, there is a distinct small vortex again in the chamber angular spaces close to the film hole close to the upper and lower wall positions.



(a) Polygonal impingement chamber



(b) Curved impingement chamber

Fig. 11 Streamline distribution and velocity contour at the center section of composite cooling structures with different shapes of impingement chambers

Analyzing the cold flow within differently shaped chamber, in the triangle, hexagon and trapezium chambers, the cold flow close to the lower wall of the vortex flows out of the vortex, and then is squeezed by the cold flow from the upper wall to the film hole, and turns to the side wall near the film hole. The momentum of the cold flow close to the lower wall in the hexagon chamber is higher. Also considering distribution of high momentum regions within chamber, the rectangular chamber is located on the upper wall impacted by the cold flow and presents as a rectangle, while the triangular, hexagonal and trapezoidal chambers are located at the periphery of the vortex. In the distribution of low momentum region in the film hole, the low momentum region in the hexagon chamber is close to the wall of the film hole and has the smallest area, whereas the regions in other chambers do not completely fit the wall of the film hole. Furthermore, the triangle chamber exhibits the largest low momentum area.

The vortex distribution in the curved impingement chamber is similar to that in the polygonal impingement chamber, and the vortex is generated by the cold flow near the negative *x* side wall from Fig. 11 (b). The vortex core in the circle chamber is located in the center, and has the greatest intensity. The vortices in flat-key and semicircle chambers are closer to the lower wall, and the

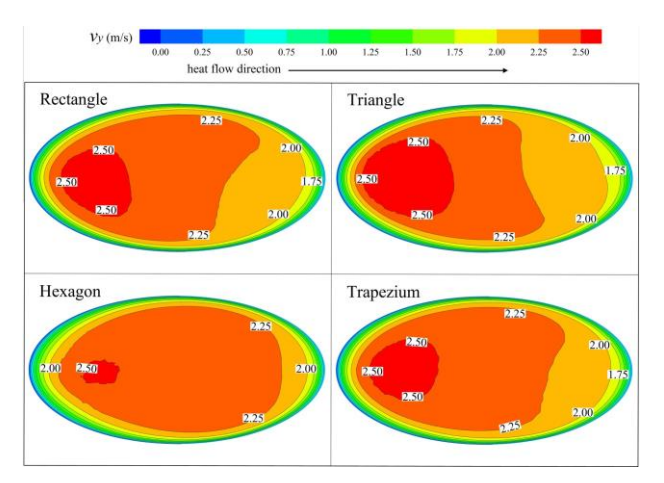
vortex intensity in flat-key chamber is intense. The vortex in the ellipse chamber is smaller. Besides, another vortex with a lower core is formed on the curved side wall near the film hole and is more powerful than the one in the negative  $\boldsymbol{x}$  direction.

Observing the cold flow inside the curved chamber, the cold flow pattern in the circle, ellipse and flat-key chambers is consistent with that in the triangle, hexagon and trapezium polygonal chambers. The cold flow close to the lower wall in the circle chamber has a larger momentum, and the vortex inside the elliptical chamber is formed by the backflow of stream towards the side wall. For the distribution of high-momentum regions, the semicircle is similar to rectangular chambers, while the rest of the chambers are comparable to each other. For the distribution of low momentum region, the circle chamber is close to the wall of film hole, and its area is the smallest, while the semicircle chamber is the largest. The ellipse, flat-key and semicircle chambers are not fully attached to the wall.

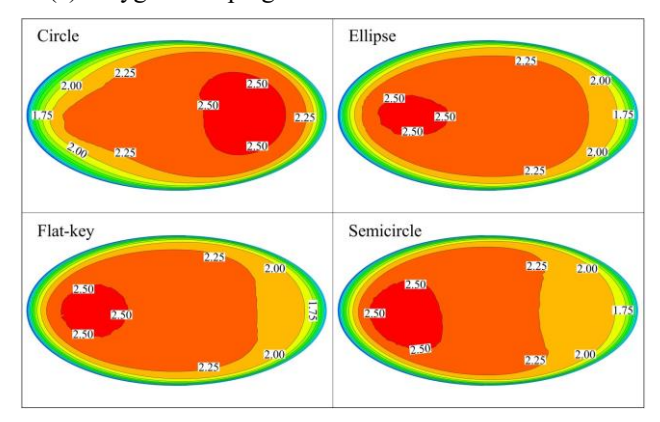
As presented in Fig. 12(a), the velocity distribution in y direction at the outlet section of the film hole of composite cooling structures with different shapes of polygonal impingement chambers is shown. The four polygonal impingement chambers exhibit comparable area of low momentum regions, with the largest being the triangular chamber, followed by rectangle and trapezium chambers, while the hexagon chamber shows the smallest extent. The low momentum regions of the triangle, rectangle and trapezium chambers show an asymmetric distribution with a narrow front and a wide back along the flow direction, while the hexagon chamber exhibits a symmetric distribution. Comparison of the high momentum region area shows that the hexagon chamber is the smallest, the trapezium is about four times the size of the hexagon, the rectangle chamber has a larger high momentum region, and the triangle has the largest area.

The low momentum areas of the four curved impingement chambers are approximately equivalent, of which the low momentum area of the semicircle chamber is the largest, and the circle, ellipse and flat-key chambers are slightly smaller from Fig. 12(b). The low momentum region of the ellipse, flat-key and semicircle chambers is narrow upstream and wide downstream around the film hole, whereas the circle chamber exhibits the opposite distribution. Comparing the high momentum regions of different curved impingement chambers, the order of area is circle, semicircle, flat-key and ellipse. The high momentum region of circle chamber is about twice as large as that of ellipse.

By comparing Fig. 11 with Fig. 12, the area of the downstream low momentum region of the film hole outlet section of the impingement chamber with different shapes is same as the region in the film hole. A comprehensive comparison of the high momentum region position of the film hole outlet section for eight different shapes of impingement chambers shows that the circle chamber is located downstream of the film hole outlet section, while the other chambers are the opposite. In Fig. 11, the distribution of the high momentum area in



# (a) Polygonal impingement chamber

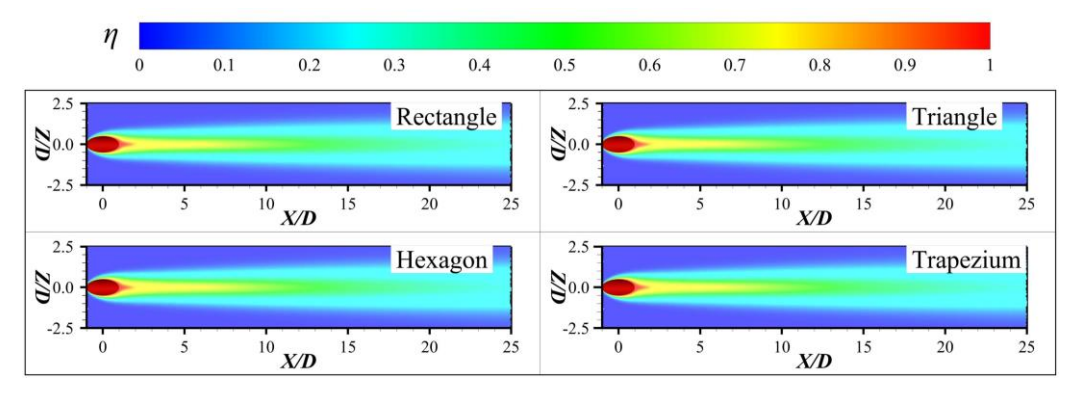


(b) Curved impingement chamber

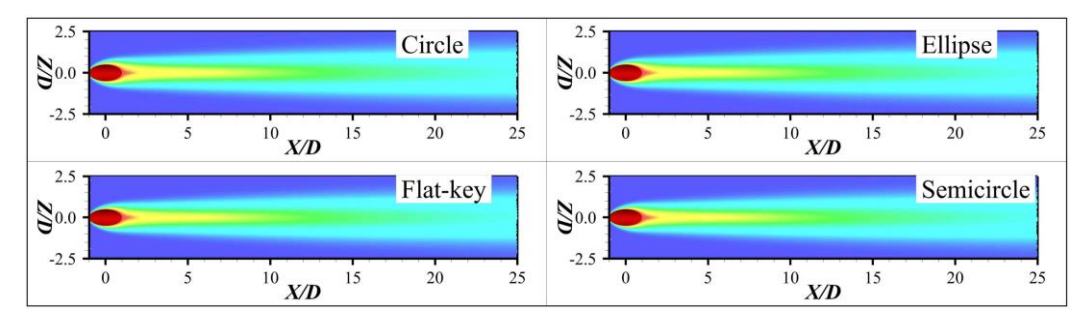
Fig. 12 Velocity distribution in the y direction at the outlet section of film hole of composite cooling structures with different shapes of impingement chambers

the rectangular and semicircle impingement chambers is similar. The area of the high momentum area in the latter chamber is slightly larger than that in the former, which is consistent with the size of the red area in Fig. 12. The distribution structure of the high momentum region of the impingement chamber with other shapes is similar in Fig. 11. According to the magnitude relationship of the cold flow momentum near the lower wall, the order is as follows: circle, hexagon, ellipse, flat-key, trapezium, triangle. In Fig. 12, the order of the area of the high momentum region of the last five chambers is exactly the opposite. There is a larger area of the high-momentum region in the circle chamber. This may be caused by the fact that the cold flow direction near the lower wall in impingement chamber is different from the other chambers.

As indicated in Fig. 13, the cooling effect of the air film in the area with X/D < 10 on the flat plate wall changes obviously. Observing the red and yellow areas at the outlet of the film hole, the shape and size of the red area of cooling effectiveness of plate wall of the polygonal impingement chamber are basically the same. The yellow area of the hexagon chamber is wider in the spreading coverage area, and the yellow region of the triangle chamber is the slimmest. The shape and size of



(a) Polygonal impingement chamber



(b) Curved impingement chamber

Fig. 13 Cooling effectiveness cloud of flat plate wall of composite cooling structures with different shapes of chambers

the red area of the cooling effectiveness of the flat wall of the curved impingement chamber show a high degree of consistency in different designs. The yellow area of the circle chamber covers a wide area in the spreading direction, while the yellow area of the semicircle chamber is relatively slender.

According to the distribution curves of average cooling effectiveness along the flow direction of composite cooling structures with different shapes of chambers in Fig. 14, the chamber shape has little effect on the cooling effectiveness distribution of the composite cooling structure on the plate wall. Across the flat plate wall, the average cooling effectiveness of circle chamber is the highest, and the remaining chambers have little difference in average cooling effectiveness. Comparing the cooling effectiveness in the area of 1 < X/D < 25, the average cooling effectiveness curve of triangle chamber is at the bottom, and the curve of hexagon chamber is only below the circle. The difference between the curves of other shapes of chambers is very small, which is between the curves of hexagon and triangle. In the region of 1<X/D<50, compared with rectangle, the surfaceaveraged cooling effectiveness of triangle, trapezium, flat-key and semicircle decreased by approximately 0.50%, 0.11%, 0.05% and 0.18%, respectively. The surface-averaged cooling effectiveness of hexagon, circle and ellipse increased by about 0.81%, 1.89% and 0.18%, respectively. In the 1<X/D<25 region, compared with rectangle, the surface-averaged cooling effectiveness of triangle, trapezium and semicircle decreased by approximately 0.67%, 0.09% and 0.26%, respectively. The surface-averaged cooling effectiveness of hexagon, circle, ellipse and flat-key increased by about 1.19%, 2.71%, 0.37% and 0.01%, respectively.

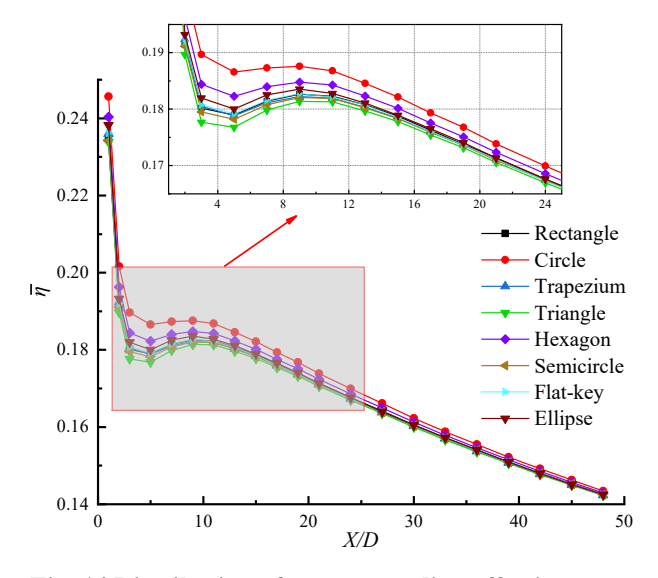


Fig. 14 Distribution of average cooling effectiveness along the flow direction of composite cooling structures with different shapes of chambers

Combining Fig. 12 with Fig. 13 shows that the area of the high momentum region of the hexagon chamber is the smallest, while the triangle and circle chambers both have the largest high momentum regions, and there is not much difference between the rest of other shapes. In the cooling effectiveness cloud, the yellow areas of circle and hexagon chambers cover a relatively wide range in the spreading direction, the yellow areas of triangle are the slenderest, and the yellow regions of the other five have little difference. Comparing the effectiveness curves of seven different shapes of chambers except for the circle, the average cooling effectiveness of the hexagon chamber is the highest,

while that of the triangle chamber is the worst, and the remaining five fall somewhere in between. This is consistent with the rule obtained in Section 3.1, that is, the larger the range of high momentum area at the outlet of the film hole, the worse the film cooling effect. The film cooling effect on the flat wall of the circle chamber is the best, which indicates that the y direction velocity distribution structure of the cold flow at the exit of the film hole has a great influence on the film cooling effectiveness on the flat wall. When the high momentum region is located downstream of the film hole exit section, the film cooling effect is better.

# 3.3 Investigation of the Effect of the Number of Cooling Units on the Cooling Flow of composite Cooling Structure

When the composite cooling structure exists alone, the cooling air film formed can only protect a portion of the downstream area of the film hole. In the actual gas turbine, the array arrangement composite cooling structure is the most common solution to extend the coverage of the cooling air film. In this section, the composite cooling structure obtained in the previous section is taken as a cooling unit to clarify the influence of the number of cooling units on the cooling film flow.

## 3.3.1 Physical Model

The cooling units are arranged along the flow direction, and the cooling unit flow distance  $L_u$  is defined as the flow distance between the centers of the film holes of two cooling units, where  $L_u$ =5D. The main flow chamber dimensions remain unchanged, the size of the cooling unit is consistent with that of the circle impingement chamber in Section 3.2, and the blowing ratio BR=2.

# 3.3.2 Effect of the Number of Cooling Units on Cooling Flow

In this section, the cooling flow of the composite cooling structure with the number of cooling units increased from  $N_u$ =1 to  $N_u$ =4 is simulated.

As shown in Fig. 15, since the cold flow structure in each impingement chamber is basically the same, they have nearly identical the velocity contour and streamline distribution. With the increase of the number of cooling units, there is a certain rule of the cold flow structure on the plate wall, that is, the cold flow from the film hole of the latter cooling unit will be wrapped by the previous cold flow. Observation of the velocity contour on the plate wall shows that there is a region of low momentum on the plate wall between the two cooling units.

The serial number in the upper left corner of Fig. 16 refers to the cooling unit of the specific composite cooling structure. For example, 4-3 represents the outlet section of film hole of the third cooling unit corresponding to the four cooling units in the figure. The high momentum region of the cold flow at the exit section of the film hole of the first cooling unit of each composite cooling structure is located downstream of the film hole from Fig. 16(a). Obviously, the area of the 2-1 high momentum region is slightly larger than the other

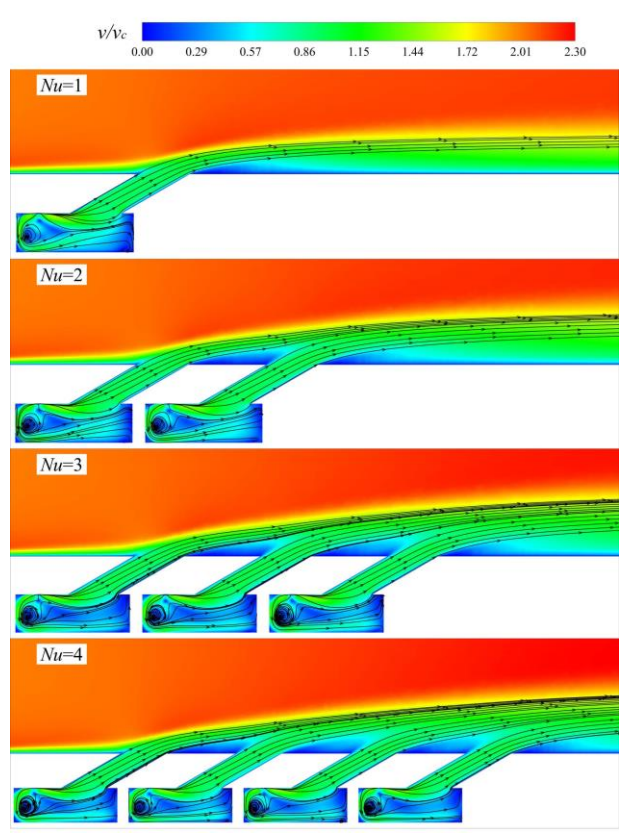
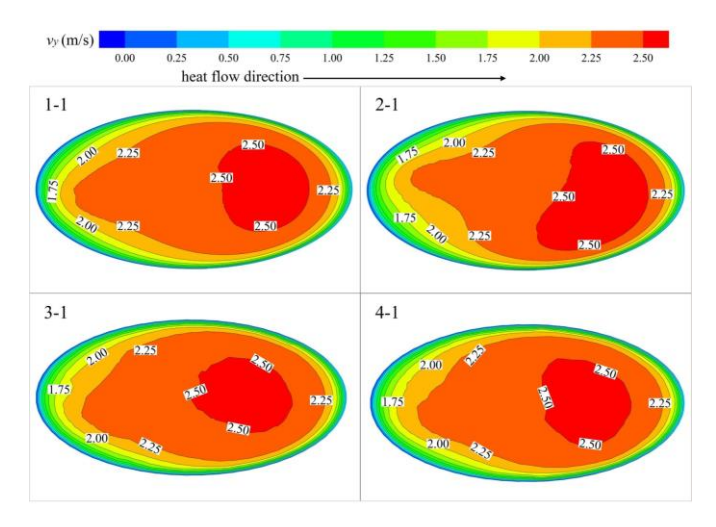


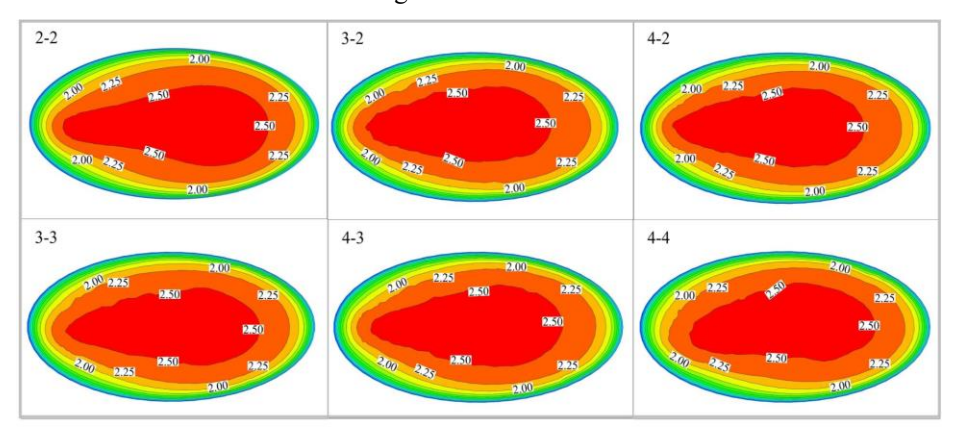
Fig. 15 Streamline distribution and velocity contour at the center section of composite cooling structures with different numbers of cooling units

three sections. The velocity distribution in the *y* direction of the cold flow at the exit section of the film hole of each composite cooling structure cooling unit is similar from Fig. 16(b). The shape of the high momentum region is comparable to that of water droplets, which is different from the velocity distribution at the film hole outlet section of the first cooling unit. Although the cold flow in the cooling unit is almost uniform, the velocity distribution in the *y* direction of the cold flow in the exit section of the film hole is not the same, indicating that the cold flow structure in the film holes is affected by the state of the nearby flow field.

The flow direction cross-section in Fig. 17(a) is located at the lower edge of the film hole outlet of the first cooling unit. The streamline distribution of the cold flow of each composite cooling structure is consistent after being ejected from the film hole, that is, the cold flow state is similar. The flow direction section in Fig. 17(b) is located at the lower edge of the film hole outlet of the second cooling unit. The flow line distribution is the same for the remaining number of cooling unit structures except for  $N_u=1$ . The vortex cores of the kidney-shaped vortex pair of  $N_u$ =1 leave the wall due to the absence of the other incoming cold flows, and the second cold flow of other composite cooling structures causes the vortex cores of the kidney-shaped vortex pair to reattach to the wall. The flow section in Fig. 17(c) is located between the film holes of the second and third cooling units. The vortex cores of kidney-shaped vortex pair also leave the wall at  $N_u=2$ , and the distribution structure of cold flow streamline is consistent for  $N_u=3$ 



(a) Outlet section of the film hole for the first cooling unit



(b) Outlet section of film holes for the remaining cooling units

Fig. 16 Velocity distribution in the *y* direction at the outlet section of film hole of composite cooling structures with different numbers of cooling units

and  $N_u$ =4. The flow direction section in Fig. 17(d) is located in the center of the film hole outlet of the fourth cooling unit. At this time, the distribution structure of the cold flow streams for  $N_u$ =3 and  $N_u$ =4 is no longer consistent, and the kidney-shaped vortex pair on both sides of the cold flow for  $N_u$ =4 are destroyed.

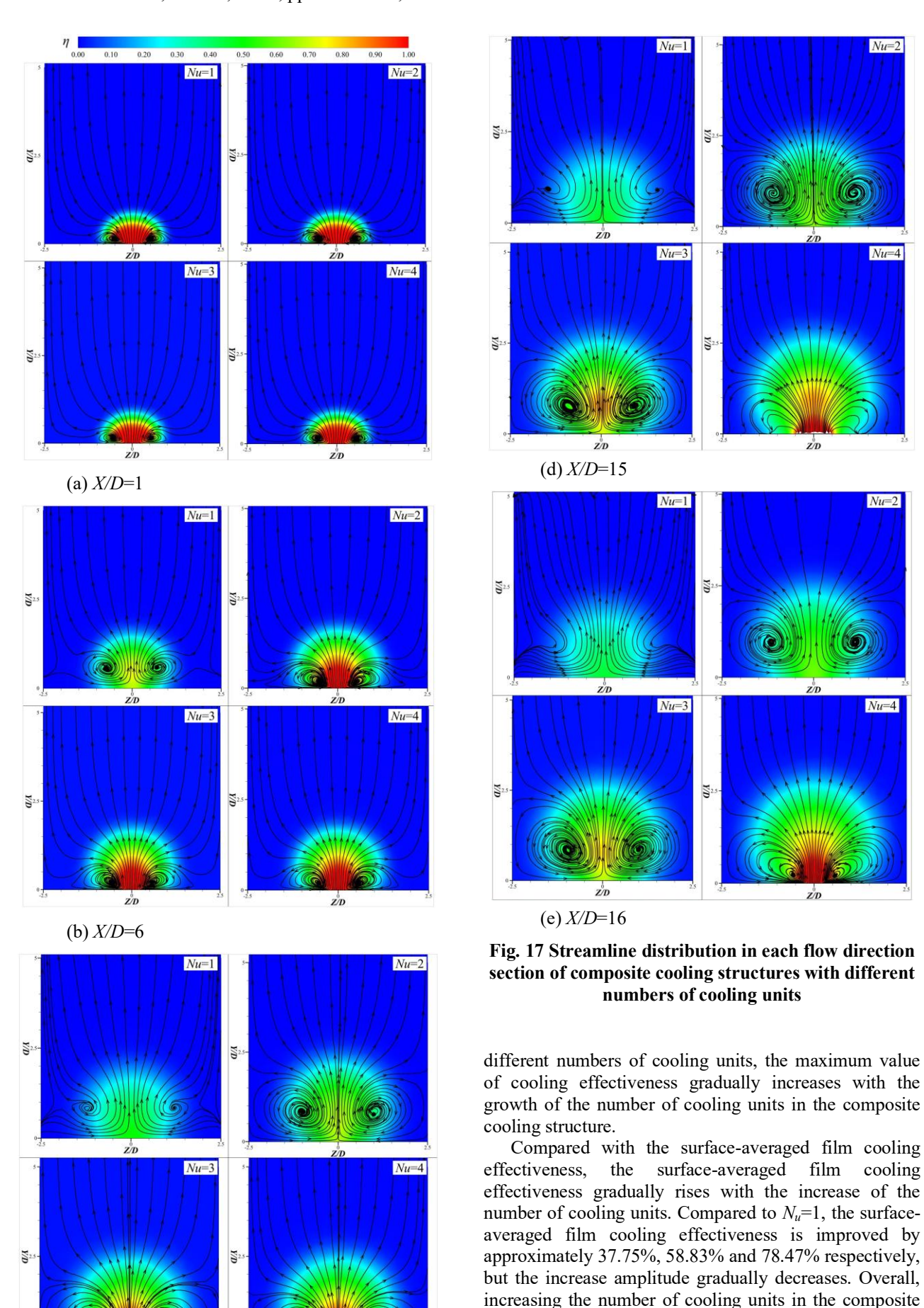
The flow section of Fig. 17(e) is located at the lower edge of the film hole outlet of the fourth cooling unit. The kidney-shaped vortex pair at  $N_u$ =4 is re-formed by the fourth cold flow. By comparing Fig. 17(c), (d), and (e), the kidney-shaped vortex pair structure in the extended film is disrupted by the cold flow ejected from the film hole of the fourth cooling unit, with a new kidney-shaped vortex pair being generated through this interaction.

With the increase of the cooling units, the cold flow from the downstream film holes will expand the coverage of the air film and enhance the cooling effect of the film. In conjunction with Fig. 16, the high momentum region at the outlet section of the film hole appears as a water droplet. This is because the cold flow from the downstream cooling unit is subjected to the pressure of the extended cooling air film when it is sprayed out.

As shown in Fig. 18, when  $N_u$ =1, only the central area of the plate wall is covered by the cooling film, and

the yellow area of the cooling film extends to about X/D=10. In the range of 25 < X/D < 50, the cooling film gradually shrinks toward the coverage area. Compared with  $N_u=1$ , with the number of cooling units increases, the yellow area of the cooling film extends to X/D=18, X/D=25 and X/D=32, respectively, and the cooling film in the wall area with 25 < X/D < 50 gradually widens. The cooling film covers almost the entire wall of the area at  $N_u=4$ . In general, increasing the number of cooling units in the composite cooling structure can broaden the coverage area of the cooling film and improve the cooling effect of the film.

Figure 19 depicts the distribution of average cooling effectiveness along the flow direction for composite cooling structures with different numbers of cooling units. The gray bar in the figure represents the position of the film hole on the wall of the flat plate. In the region of 1 < X/D < 5, when  $N_u = 1$ , the cooling effectiveness decreases sharply with the extension of the air film. The reason that the film cooling effectiveness in other cases shows a trend of a sharp decrease and then a rapid increase is the cold flow of the second cooling unit is squeezed by the extended cooling film, forming a new one. A similar trend of cooling effectiveness is also seen in the areas of 5 < X/D < 10 and 10 < X/D < 15. By observing the maximum value of average cooling effectiveness of



(c) X/D=13

wall region.

cooling structure will significantly enhance the ductility and cooling performance of the film in the downstream

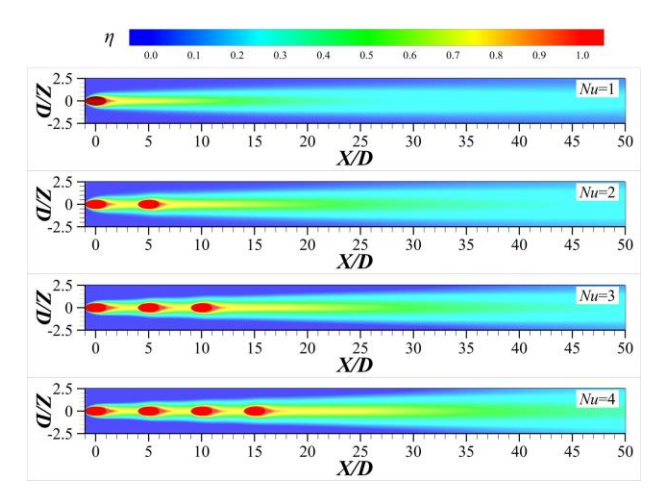


Fig. 18 Cooling effectiveness cloud of flat plate wall of composite cooling structures with different number of cooling units

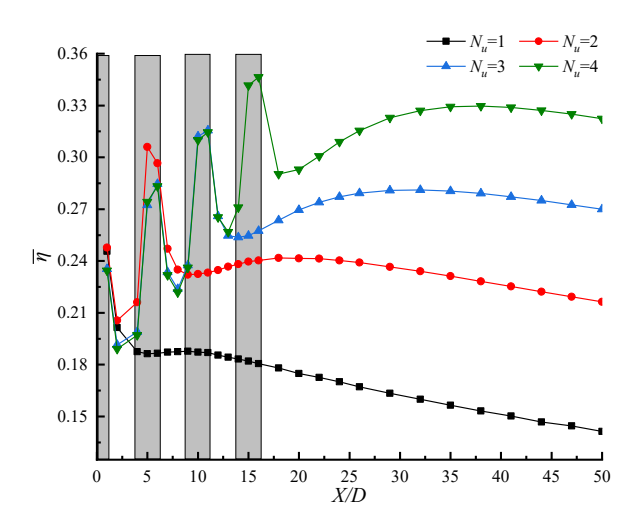


Fig. 19 Distribution of average cooling effectiveness along the flow direction for composite cooling structures with different numbers of cooling units

### 4. CONCLUSION

In this paper, the finite volume composite cooling structure is taken as the research object to analyze the correlation between internal cooling flow and external cooling effect. The main results are as follows:

(1) The effect of the volume of the impingement chamber of a composite cooling structure on the cooling flow is investigated. The results show that the cold flow in the impingement chambers with different volumes is constrained by the side wall of the chamber, which affects the cold flow state in the film hole. The larger the area of the low momentum region of the cold flow on the wall of the film hole, the greater the area of the low momentum region of the cold flow at the exit section of the film hole. By comparing the velocity distribution in the y direction of the cold flow at the exit section of the film hole, it is found that the high momentum region is mainly distributed on the upper wall of the film hole. The intensity of the kidney-shaped vortex pair on both sides of the cold flow increases with the area of high momentum region, resulting in poorer air

attachment. The surface-averaged film cooling effectiveness of the composite cooling structure at  $0.8V_r$  increases by about 3.96% compared to  $1.0V_r$ .

- (2) By simulating the cold flow of the composite cooling structure with different shapes of impingement chambers, it is found that the direction of the cold flow close to the lower wall in the circular chamber is different from that in other shapes of chambers. This leads to a unique velocity distribution in the y direction of the cold flow at the outlet of the film hole. The high momentum region is located downstream of the film hole outlet section, and its air film adhesion is slightly better than that in other shapes of chambers. The surface-averaged film cooling effectiveness of the flat wall of the circular chamber has improved by approximately 1.89% compared to the rectangular chamber.
- (3) The cooling structure is regarded as a cooling unit, and the influence of different numbers of cooling units on the cooling flow is investigated. It is found that, except for the first cooling unit, the high momentum region of the cold flow at the exit section of the film holes in other cooling units is water droplets, which is caused by the extrusion deformation of the air film on the wall when the cold flow is ejected. In addition, the added cooling unit will reconstruct the flow structure of the air film, enhance the ductility and wall adhesion of the air film, and improve the cooling effect of the air film. The surface-averaged film cooling effectiveness is elevated by about 78.47% at  $N_u$ =4 compared to  $N_u$ =1.

It is imperative to acknowledge that the aforementioned enhancement in cooling efficiency is derived from a numerical model of a hypothetical nature, and the actual manufacturing tolerance and other factors may introduce additional uncertainty. Industrial applications need to be verified by experiments under engine related working conditions.

Finally, dynamic factors such as transient fluctuation of heat flow and main stream pressure fluctuation in actual working conditions are not included in the model boundary conditions of this study. Meanwhile, the solid wall conduction and other factors are not considered, which may be partially different from the real working conditions. Although the Realizable k- $\varepsilon$  turbulence model can accurately predict the jet diffusion characteristics, it still has accuracy limitations. In the future, the impingement-film composite cooling test bench can be built, and the numerical model can be verified by experimental means. Additionally, the cooling structure can be applied to the high heat load area such as the leading edge of turbine blade to carry out engineering practical verification.

# **CONFLICT OF INTEREST**

The author has no conflicts to disclose.

### **AUTHORS CONTRIBUTION**

Junhui Liu: Writing original draft; Zhipeng Zhu: Validation; Jianlong Chang: Writing-review, Project

administration; **Shuai Ma**: Investigation; **Jiahao Sun**: Data Curation.

### REFERENCES

- Boyce, M. P. (2011). An Overview of Gas Turbines. *Gas turbine engineering handbook*. Elsevier. <a href="https://doi.org/10.1016/B978-0-12-383842-1.00001-9">https://doi.org/10.1016/B978-0-12-383842-1.00001-9</a>
- Bunker, R. S. (2005). A review of shaped hole turbine film-cooling technology. J. Heat Transfer, 127(4), 441-453. https://doi.org/10.1115/1.1860562
- Bunker, R. S. (2007). Gas Turbine Heat Transfer: Ten Remaining Hot Gas Path Challenges. *Journal of Turbomachinery*, 129(2), 193–201. https://doi.org/10.1115/1.2464142
- Cheng, X., Li, Z. R., Wan, H. N., Ji, W. T., He, Y. L., & Tao, W. Q. (2023). Effect of mass flow ratios on the conjugate heat transfer of a metal turbine vane at medium temperature. *International Journal of Heat and Mass Transfer*, 209, 124096. <a href="https://doi.org/10.1016/j.ijheatmasstransfer.2023.12">https://doi.org/10.1016/j.ijheatmasstransfer.2023.12</a> 4096
- Cho, H. H., & Rhee, D. H. (2001). Local heat/mass transfer measurement on the effusion plate in impingement/effusion cooling systems. *J. Turbomach.*, *123*(3), 601-608. https://doi.org/10.1115/1.1344904
- El-Jummah, A. M., Nazari, A., Andrews, G. E., & Staggs, J. E. (2017, June). Impingement/Effusion Cooling Wall Heat Transfer: Reduced Number of Impingement Jet Holes Relative to the Effusion Holes. In *Turbo Expo: Power for Land, Sea, and Air* (Vol. 50893, p. V05CT17A005). American Society of Mechanical Engineers. <a href="https://doi.org/10.1115/GT2017-63494">https://doi.org/10.1115/GT2017-63494</a>
- Kalghatgi, P., & Acharya, S. (2015). Improved film cooling effectiveness with a round film cooling hole embedded in a contoured crater. *Journal of Turbomachinery*, 137(10), 101006. https://doi.org/10.1115/1.4030395
- Li, F., Wang, H., Liu, Z., Feng, Z., & Shi, Y. (2022). Comparisons of blade tip phantom cooling effectiveness for two tip structures with three tip clearances. *Applied Thermal Engineering*, 202, 117868. <a href="https://doi.org/10.1016/j.applthermaleng.2021.117868">https://doi.org/10.1016/j.applthermaleng.2021.117868</a>
- Li, W., Li, X., Ren, J., & Jiang, H. (2017). Large eddy simulation of compound angle hole film cooling with hole length-to-diameter ratio and internal crossflow orientation effects. International Journal of Thermal Sciences, 121, 410-423. https://doi.org/10.1016/j.ijthermalsci.2017.08.001
- Ligrani, P. M., Ren, Z., & Buzzard, W. C. (2017). Impingement jet array heat transfer with small-scale cylinder target surface roughness arrays. *International Journal of Heat and Mass Transfer*,

- 107, 895-905. <a href="https://doi.org/10.1016/j.ijheatmasstransfer.2016.10.">https://doi.org/10.1016/j.ijheatmasstransfer.2016.10.</a>
- Liu, X., Zhang, C., Song, L., & Li, J. (2021). Influence of Biot number and geometric parameters on the overall cooling effectiveness of double wall structure with pins. *Applied Thermal Engineering*, 198, 117439. <a href="https://doi.org/10.1016/j.applthermaleng.2021.1174">https://doi.org/10.1016/j.applthermaleng.2021.1174</a>
- Liu, Y., Rao, Y., & Yang, L. (2020). Numerical simulations of a double-wall cooling with internal jet impingement and external hexagonal arrangement of film cooling holes. *International Journal of Thermal Sciences*, 153, 106337. https://doi.org/10.1016/j.ijthermalsci.2020.106337
- Liu, Y., Rao, Y., Yang, L., Xu, Y., & Terzis, A. (2021). Flow and heat transfer characteristics of double-wall cooling with multi-row short film cooling hole arrangements. *International Journal of Thermal Sciences*, 165, 106878. https://doi.org/10.1016/j.ijthermalsci.2021.106878
- Liu, Z., Li, F., Zhang, Z., Feng, Z., & Simon, T. W. (2021). Conjugate heat transfer predictions on combined impingement and film cooling of a blade leading edge model. *Heat Transfer Engineering*, 42(16), 1363-1380. https://doi.org/10.1080/01457632.2020.1794625
- Luan, Y., Rao, Y., & Yan, H. (2023). Experimental and numerical study of swirl impingement cooling for turbine blade leading edge with internal ridged wall and film extraction holes. *International Journal of Heat and Mass Transfer*, 201, 123633. <a href="https://doi.org/10.1016/j.ijheatmasstransfer.2022.12">https://doi.org/10.1016/j.ijheatmasstransfer.2022.12</a>
- Luo, L., Wang, C., Wang, L., Sunden, B. A., & Wang, S. (2016). A numerical investigation of dimple effects on internal heat transfer enhancement of a double wall cooling structure with jet impingement. International Journal of Numerical Methods for Heat & Fluid Flow, 26(7), 2175-2197. http://dx.doi.org/10.1108/HFF-02-2015-0081
- Nathan, M. L., Dyson, T. E., Bogard, D. G., & Bradshaw, S. D. (2014). Adiabatic and overall effectiveness for the showerhead film cooling of a turbine vane. *Journal of Turbomachinery*, *136*(3), 031005. <a href="https://doi.org/10.1115/1.4024680">https://doi.org/10.1115/1.4024680</a>
- Nourin, F. N., & Amano, R. S. (2021). Review of gas turbine internal cooling improvement technology. *Journal of Energy Resources Technology*, *143*(8), 080801. https://doi.org/10.1115/1.4048865
- Ravelli, S., Dobrowolski, L., & Bogard, D. G. (2010, October). Evaluating the effects of internal impingement cooling on a film cooled turbine blade leading edge. In *Turbo Expo: Power for Land, Sea, and Air* (Vol. 43994, pp. 1655-1665), Glasgow, UK. https://doi.org/10.1115/GT2010-23002
- Schmidt, D. L., Sen, B., & Bogard, D. G. (1996). Film

cooling with compound angle holes: adiabatic effectiveness. https://doi.org/10.1115/1.2840938

Seok, W., Heo, Y. M., & Rhee, S. H. (2024). Performance enhancement of a vortex ring thruster by adopting the Coanda effect. Journal of Marine Science and Technology, 29(3), 683-695. https://doi.org/10.1007/s00773-024-01014-2

Singh, K. (2022). Combined film and impingement cooling of flat plate with reverse cooling hole. Applied Thermal Engineering, 208, 118224. https://doi.org/10.1016/j.applthermaleng.2022.1182

Unnikrishnan, U., & Yang, V. (2022). A review of cooling technologies for high temperature rotating components in gas turbine. *Propulsion and Power Research*, 11(3), 293-310. https://doi.org/10.1016/j.jppr.2022.07.001

Xiao-ming, T., Jing-zhou, Z., & Hua-sheng, X. (2015). Experimental investigation on impingement/effusion cooling with short normal injection holes. *International Communications in Heat and Mass Transfer*, 69, 1-10. <a href="https://doi.org/10.1016/j.icheatmasstransfer.2015.09">https://doi.org/10.1016/j.icheatmasstransfer.2015.09</a>

Yang, L., Kan, R., Ren, J., & Jiang, H. (2013, June). Effect of film cooling arrangement on impingement heat transfer on turbine blade leading edge. In *Turbo Expo: Power for Land, Sea, and Air* (Vol. 55140, p. V03AT12A037). American Society of Mechanical Engineers. <a href="https://doi.org/10.1115/GT2013-95261">https://doi.org/10.1115/GT2013-95261</a>

Yang, W., Pu, J., & Wang, J. (2016). The combined effects of an upstream ramp and swirling coolant flow on film cooling characteristics. *Journal of Turbomachinery*, 138(11), 111008. https://doi.org/10.1115/1.4033292

Yeranee, K., & Yu, R. A. O. (2021). A review of recent studies on rotating internal cooling for gas turbine blades. *Chinese Journal of Aeronautics*, *34*(7), 85-113. <a href="https://doi.org/10.1016/j.cja.2020.12.035">https://doi.org/10.1016/j.cja.2020.12.035</a>

Zhang, J., Zheng, Q., Xu, J., Yue, G., & Jiang, Y. (2023).

Conjugate heat transfer and flow analysis on double-wall cooling with impingement induced swirling and film cooling. *Applied Thermal Engineering*, 223, 120014.

<a href="https://doi.org/10.1016/j.applthermaleng.2023.1200">https://doi.org/10.1016/j.applthermaleng.2023.1200</a>

Zhang, R., Luo, C., Zhou, L., Li, L., Zhang, H., & Du, X. (2022). Impingement/film cooling of C3X vane with double-wall cooling structure using air/mist mixture. *International Journal of Heat and Mass Transfer*, 188, 122594. https://doi.org/10.1016/j.ijheatmasstransfer.2022.12 2594

#### APPENDIX A

The transport equations of turbulent kinetic energy and turbulent dissipation rate of the Realizable k- $\varepsilon$  model are shown below. The following equation retains the general form of the transient term  $(\partial/\partial t)$ . The steady-state simulation is adopted in this paper, and the transient term disappears in the convergent solution  $(\partial/\partial t=0)$ , which is included in the standard form of the equation.

$$\frac{\partial(\rho k)}{\partial t} + \frac{\partial(\rho k u_j)}{\partial x_j} = \frac{\partial}{\partial x_j} \left[ \left( \mu + \frac{\mu_t}{\sigma_k} \right) \frac{\partial k}{\partial x_j} \right] + G_k + G_b - \rho \varepsilon - Y_M + S_k$$
 (1)

$$\frac{\partial(\rho\varepsilon)}{\partial t} + \frac{\partial(\rho\varepsilon u_{j})}{\partial x_{j}} = \frac{\partial}{\partial x_{j}} \left[ \left( \mu + \frac{\mu_{t}}{\sigma_{\varepsilon}} \right) \frac{\partial\varepsilon}{\partial x_{j}} \right] + \rho C_{1}S\varepsilon - \frac{\rho C_{2}\varepsilon^{2}}{k + \sqrt{\varepsilon v}} + C_{\varepsilon 1} \frac{\varepsilon}{k} C_{\varepsilon 3}G_{b} + S_{\varepsilon} (2)$$

where 
$$C_1 = \max \left[ 0.43, \frac{\eta}{\eta + 5} \right], \eta = S \frac{k}{\varepsilon}, S = \sqrt{2S_{ij}S_{ij}}$$

In these equations, k and  $\varepsilon$  represent the turbulent kinetic energy and turbulent dissipation rate,  $G_k$  is the turbulent kinetic energy generated by the mean velocity gradient,  $G_b$  is the turbulent kinetic energy caused by buoyancy effect,  $\mu$  is the viscosity coefficient,  $\mu_t$  is the turbulent viscosity coefficient, respectively.  $Y_M$  stands for the contribution of pulsating expansion to the total dissipation rate in compressible turbulence,  $C_2$  and  $C_{1\varepsilon}$  are constants.  $\sigma_k$  and  $\sigma_\varepsilon$  are the turbulent Prandtl numbers for k and  $\varepsilon$ , respectively.  $S_k$  and  $S_\varepsilon$  are user-defined source terms.

# APPENDIX B

Some of the terms and parameters used in this article are defined as follows.

Cooling flow ductility: the ability of the cooling flow to extend and maintain continuity along the wall after leaving the film hole is evaluated by the space coverage and adhesion duration of the cooling film.

Kidney-shaped vortex pair: A specific vortex form formed in fluid dynamics is a pair of rotating vortices with kidney shaped structure, which affects the film cooling adhesion.

Cooling unit: A basic module consisting of an impact hole, an impingement chamber, and an air film hole.

Flow direction: Consistent with the direction of mainstream movement, it is the "forward direction" of flow.

Normal direction: Perpendicular to the wall or object surface, it is the "vertical direction" of flow.

Spanwise direction: Perpendicular to both the flow direction and the normal direction, typically corresponding to the "lateral expansion direction" of the flow.

The blowing ratio BR is defined as:

$$BR = \frac{\rho_c v_c}{\rho_g v_g} \tag{3}$$

Where,  $\rho_c$  and  $v_c$  represent the density and velocity of the cold flow,  $\rho_g$  and  $v_g$  are the density and velocity of the main flow, respectively.

The parameter  $\eta$  characterizing the film cooling effectiveness is defined as follow:

$$\eta = \frac{T_m - T_\omega}{T_m - T_c} \tag{4}$$

Where,  $T_m$  represents the inlet temperature of the main stream,  $T_c$  is the cold flow temperature, and  $T_{\omega}$  indicates the wall temperature.

The average film cooling effectiveness parameter  $\overline{\eta}$  characterizing a spreading position on the wall is defined

$$\overline{\eta} = \frac{1}{\Delta z} \int \eta(x, z) dz = \frac{1}{\Delta Z} \int \eta(k, z) dz$$
 (5)

Where,  $\Delta z$  represents the spreading width of the wall.  $\eta(x,z)$  is the cooling effectiveness of the point (x, z) on the wall.

The average film cooling effectiveness parameter  $\overline{\eta}_s$  characterizing a certain area on the wall is defined as the surface-averaged film cooling effectiveness, which can directly measure the quality of the cooling effect in this area, and is calculated by the formula:

$$\overline{\eta}_{S} = \frac{1}{\Delta A} \iint \eta(x, z) dx dz = \frac{1}{\Delta A} \int_{i}^{j} \overline{\eta}(n, z) dx, n \in [i, j]$$
 (6)

Where,  $\Delta A$  is the area size of the measured region and [i, j] is the interval range of the direction of flow of the measured area.